Journal of Materials Chemistry A

ROYAL SOCIETY OF CHEMISTRY

PAPER

View Article Online
View Journal | View Issue

Check for updates

Cite this: J. Mater. Chem. A, 2024, 12, 2383

Enhanced electrocatalytic hydrogen evolution in alkaline saline electrolyte by NiCo foam supported iridium nanoclusters†

Jiaxin Yuan,[a] Jinsong Zhou,[a] Zehua Peng,[ab] Gang Li,[a] Yang Hou[c] and Michael K. H. Leung[*ad]

Received 6th September 2023
Accepted 4th December 2023

DOI: 10.1039/d3ta05421g

rsc.li/materials-a

Developing high-performance hydrogen evolution reaction (HER) electrocatalysts working at a high current density is essential because of the increasing demand for clean and renewable hydrogen energy. Herein, we have developed Ir nanocluster-decorated macroporous NiCo foam (Ir-nc@m-NiCo) to overcome the sluggish HER kinetics for enhanced hydrogen production. Ir-nc@m-NiCo can be fabricated by a corrosion engineering method. In the mechanism of electron transfer from Ni and Co to Ir at the interface between the NiCo foam and Ir cluster, the electrons accumulated on Ir favor optimal adsorption of H* for the HER. Therefore, Ir-nc@m-NiCo exhibits excellent HER activity, reaching current densities of 500 and 1000 mA cm^{-2} at low overpotentials of 101 and 146 mV, respectively, in 1.0 M KOH electrolyte. Moreover, Ir-nc@m-NiCo possesses remarkable HER activity in simulated alkaline seawater electrolytes with 1000 mA cm^{-2} at 178 mV and demonstrates long-term durability with a slight potential increase after 10 hours testing under 500 mA cm^{-2}.

Electrochemical water splitting is a promising approach to generate renewable, green, and sustainable hydrogen fuel.[1–3] The hydrogen evolution reaction (HER) is the most crucial step activated by highly efficient electrocatalysts for water splitting, particularly in alkaline media.[4] Precious metal-based catalysts, such as platinum (Pt), iridium (Ir), palladium (Pa), and ruthenium (Ru), are excellent HER catalysts due to their intrinsic activity.[5–7] However, their high cost and scarcity hinder the widespread application.[6,8] To overcome these issues, diverse efforts have been made to enhance the utilization of these precious metals.[9] In reported studies, platinum was used as the benchmark, which is currently used commercially as a HER catalyst. As a neighboring element of platinum, iridium exhibits similar catalytic behavior.[10] Moreover, iridium possesses a higher catalytic potential than platinum due to its more desirable Gibbs-free energy.[11] Theoretically, increasing the number of excited atomic sites in the HER process can significantly increase the catalytic activity.[12–14] Therefore, tailoring Ir to efficient homogeneously dispersed forms of noble metals (single atoms,[15] nanoclusters,[16] or nanoparticles[11]) not only can excite the "hidden" catalytic sites, but also can reduce the noble metal content further and thus potentially increase the intrinsic activity and utilization efficiency.

Recently, metal nanoclusters have attracted researchers' attention due to their small particle size and use of small amounts of precious metals.[17] Meanwhile, metal-supported nanoclusters offer a promising approach to optimize the HER activity owing to the increased interfacial interaction between the metals and the supports.[18] To date, many materials have presented enhanced HER performance by decorating metal clusters on supported electrocatalysts, such as nickel foam,[19] carbon substrate,[20] nitride,[21] and titanium dioxide.[9] NiCo foam, as a novel support, has attracted particular attention due to its improved intrinsic catalytic activity and enhanced corrosion resistance compared to pure Ni foam and other carbon materials under alkaline conditions.[22] Besides, Ir fixed with non-metal elements can efficiently promote intrinsic catalytic activity by modifying the electron environment of Ir to tune the adsorption of active H species.[23] These combinations between Ir and non-metal elements not only tune the electron transfer pathways but also improve the utilization of precious metals. Therefore, we deduce that a small amount of iridium combined with NiCo foam may yield a stronger metal-support interaction, resulting in superior HER activity and stability.

Herein, we introduce a simple corrosion engineering method to uniformly grow a series of Ir nanoclusters on the skeleton of macroporous NiCo foam (Ir-nc@m-NiCo). The small

[a]Ability R&D Energy Research Centre, School of Energy and Environment, City University of Hong Kong, Hong Kong, China. E-mail: mkh.leung@cityu.edu.hk
[b]Department of Mechanical Engineering, College of Engineering, City University of Hong Kong, Hong Kong, China
[c]Key Laboratory of Biomass Chemical Engineering of Ministry of Education, College of Chemical and Biological Engineering, Zhejiang University, Hangzhou 310027, China
[d]State Key Laboratory of Marine Pollution, City University of Hong Kong, Hong Kong, China

† Electronic supplementary information (ESI) available. See DOI: https://doi.org/10.1039/d3ta05421g

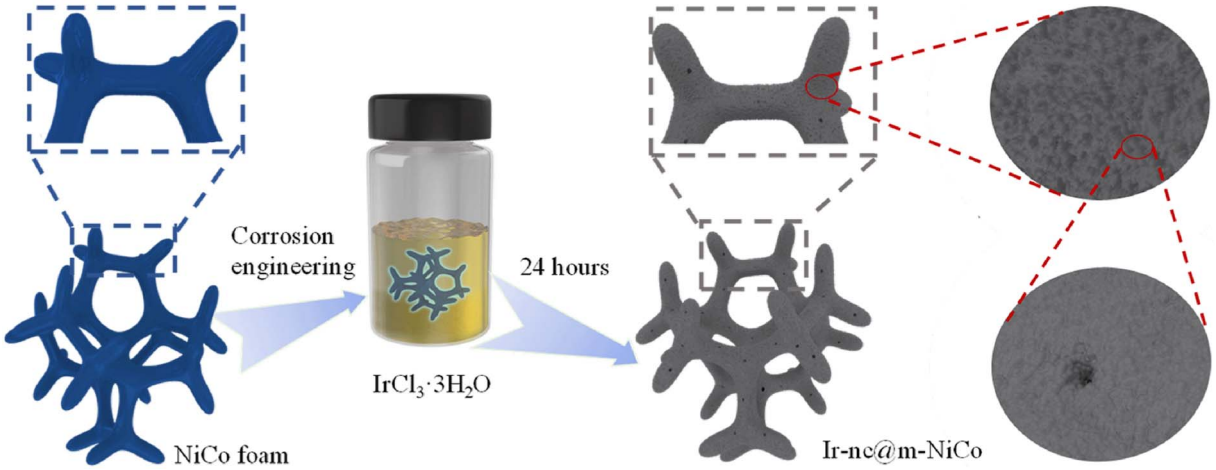

Fig. 1 Schematic illustration of the fabrication of Ir-nc@m-NiCo.

particle size and macroporous structure of Ir-nc@m-NiCo significantly promote the exposure of more active sites and, thus, boost fast electron transfer ability. As a result, Ir-nc@m-NiCo has excellent HER activity in both alkaline solution and simulated alkaline seawater electrolyte. Specifically, Ir-nc@m-NiCo exhibits outstanding HER activity, with an overpotential of 20.8 mV at a current density of 10 mA cm^{-2} in alkaline solution. First-principles calculations reveal that the weakened adsorption energy of hydrogen on Ir-nc@m-NiCo is the key to boosting the HER catalytic activity. Moreover, Ir-nc@m-NiCo continuously delivers a high current density of 500 mA cm^{-2} at a low cell voltage of only 2.05 V for an extended period of 80 hours, showing remarkable electrocatalytic activity and stability for electrocatalytic water-splitting hydrogen production.

The Ir nanoclusters supported on NiCo foam were fabricated by the corrosion method schematically illustrated in Fig. 1. Catalysts with different loadings of Ir were synthesized through different amounts of $IrCl_3 \cdot 3H_2O$, and the optimal $IrCl_3 \cdot 3H_2O$ concentration was 10 mM (Fig. S1†). The morphologies and macrostructures of Ir-nc@m-NiCo were analyzed using a field scanning electron microscope (FE-SEM) and high-resolution transmission electron microscope

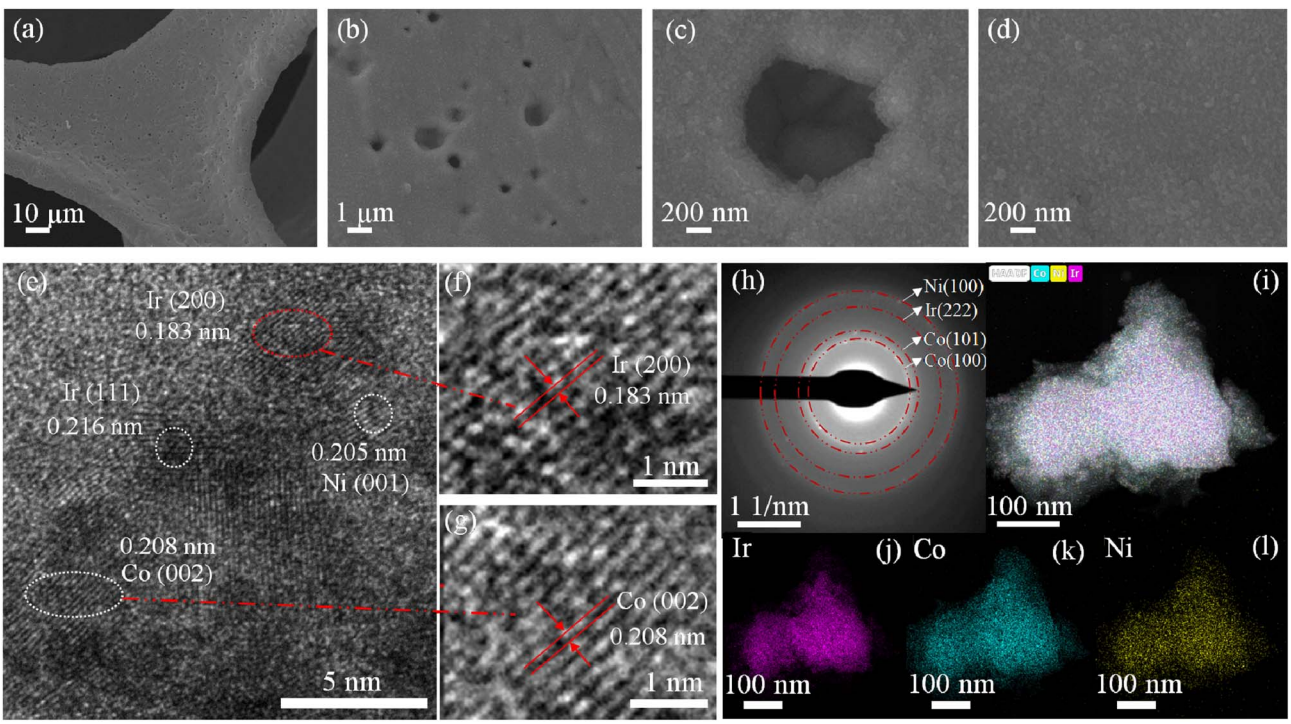

Fig. 2 (a–d) FESEM images of Ir-nc@m-NiCo. (e–g) HR-TEM images of Ir-nc@m-NiCo. (h–l) SAED pattern and EDX elemental mapping images of Ir, Co, and Ni elements in Ir-nc@m-NiCo.

(HRTEM). As shown in Fig. 2 and S2,† the corrosive effect of the $IrCl_3 \cdot 3H_2O$ solution yields uniform Ir nanoclusters decorated on the surface of the NiCo skeleton with varied sizes of macropores (>50 nm). The diameters of macropores on the NiCo foam are around 100–1000 nm (Fig. 2b). As shown in the high-resolution TEM images, the Ir nanoclusters, marked with red circles in Fig. S3,† are uniformly distributed within the NiCo substrate. The lattice fringes in Fig. 2e and f reveal a *d*-spacing of 0.183 nm, assigned to (200) with the fcc phase of Ir nanoclusters. Fig. 2e and f show lattice spacings of 0.208 and 0.205 corresponding to the Co (002) and Ni (011) planes of Ir-nc@m-NiCo, respectively. The corresponding selected area electron diffraction (SAED) pattern confirms that the Ir nanocluster in Ir-nc@m-NiCo is crystalline (Fig. 2e). In addition, the energy dispersive spectroscopy (EDS) results of Ir-nc@m-NiCo shown in Fig. 1i–l further reveal that the elements of Ir, Co, and Ni are distributed uniformly over the catalyst surface. The above findings confirm that the Ir clusters are homogeneously dispersed on the NiCo skeleton.

The crystal structures of Ir-nc@m-NiCo and pristine NiCo were further characterized by X-ray diffraction (XRD). As shown in Fig. 3a, the peaks shown in the black line match well with the Co (JPCDS no. 05-0727) and Ni (JPCDS no. 45-1027) of pristine NiCo. The peaks of Ni are weaker than those of Co due to the low Ni/Co molar ratio of 1 : 9 in the NiCo foam. After corrosion, the XRD pattern of Ir-nc@m-NiCo shows new peaks at 40.5° and 69.0°, matching well with Ir (JPCDS no. 02-1155), indicating that Ir was successfully deposited on the surface of NiCo foam in the form of clusters instead of Ir oxides. Meanwhile, the peaks of both Ni and Co exhibit a slight negative shift after corrosion as the Ir nanoclusters successfully coordinate with Ni and Co atoms. The slight negative variation in the XRD patterns implies that the introduction of larger Ir ions into NiCo reduces the crystalline quality and leads to lattice expansion, due to the Ir nanocluster coordination of Ni and Co atoms during the corrosion process. The HR-TEM results further confirm this analysis as they distinctly evidence the formation of the Ir cluster structure. To further provide an in-depth insight into the changes of Ir-nc@m-NiCo in the HER process and explore the

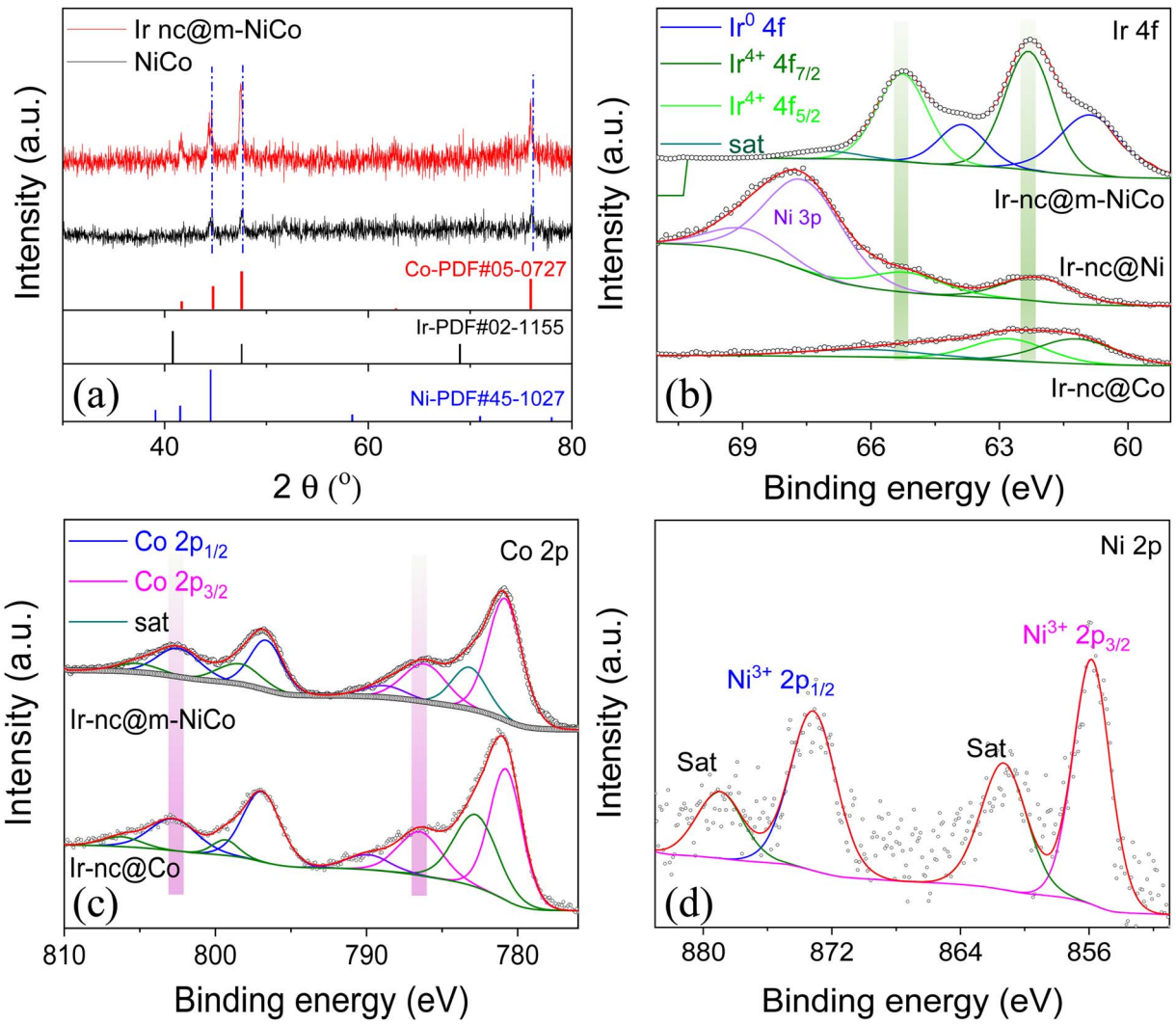

Fig. 3 (a) XRD of Ir-nc@m-NiCo. High-resolution XPS spectra of (b) Ir 4f for Ir-nc@m-NiCo, Ir-nc@Ni, and Ir-nc@Co, (c) Co 3d for Ir-nc@m-NiCo and Ir-nc@Co and (d) Ni 3d for Ir-nc@m-NiCo and Ir-nc@Ni.

active sites of the HER, X-ray photoelectron spectroscopy (XPS) was performed to analyze the surface chemical environment and valence states. The Ir content of Ir-nc@m-NiCo was further confirmed to be about 3.8 wt% *via* inductively coupled plasma (ICP) mass spectrometry. As shown in Fig. 3b, Ir in Ir-nc@m-NiCo can be fitted to Ir and Ir^{4+} species. The peaks located at 60.9 and 63.9 eV can be assigned to Ir^0. The other two peaks at 62.33 and 65.26 can be assigned to Ir^{4+} $4f_{7/2}$ and Ir^{4+} $4f_{5/2}$, respectively.[24–26] Comparing the Ir spectra of Ir-nc@m-NiCo, Ir-nc@Ni, and Ir-nc@Co, the binding energy of Ir 4f in Ir-nc@Ni and Ir-nc@Co gradually shifts to lower values. The coexistence of various valence states due to the electron transfer from Ni and Co to Ir is clarified. In Ir-nc@Ni, the peaks at 67.7 and 69.1 eV are from Ni 3p.[27] The Co 2p spectrum section has prominent peaks at 780.9 and 796.7 eV attributed to Co^{2+}, while binding energy values of 786.2 and 802.6 eV centered at Co $2p_{3/2}$ and Co $2p_{1/2}$ primary peak positions correspond to spinel Co^{3+} (Fig. 3c). It is worth noting that the Co 2p in Ir-nc@m-NiCo shows a positive shift compared with Co in Ir-nc@Co, further suggesting the electron transfer from Ni and Co to Ir. In Fig. 3d, two Ni(II) peaks are found with binding energies of 855.87 and 873.2 eV, consistent with previously reported values. Moreover, the Ni 2p also shows a positive shift in Ir-nc@m-NiCo compared with Ir-nc@Ni, verifying the electron transfer again (Fig. S4†). These results suggest the Ir coordination of Ni and Co atoms in Ir-nc@m-NiCo.

The electrocatalytic performances of the catalysts were first measured in 1.0 M KOH solution with a three-electrode cell system under room conditions. To prove the crucial contributions of the individual components in the Ir-nc@m-NiCo structure, Ir-nc@Co, Ir-nc@Ni, and Pt/C@NiCo were tested as control samples. As shown in Fig. 4a, Ir-nc@m-NiCo shows an excellent electrocatalytic activity with a small overpotential of 20.8 mV to reach a current density of 10 mA cm^{-2}, compared with Ir-nc@Co (32 mV) and Ir-nc@Ni (46 mV). For the high current density to reach 100, 500, and 1000 mA cm^{-2}, the corresponding overpotentials of Ir-nc@m-NiCo are 59, 101, and 146 mV, respectively, which are much lower than that of the benchmark catalyst Pt/C@NiCo (Fig. 4b). The Tafel slope of Ir-nc@m-NiCo is 30.8 dec^{-1} (Fig. 4c), which is much smaller than the Tafel slopes of Ir-nc@Co (47.1 dec^{-1}), Ir-nc@Ni (61.3 dec^{-1}), and Pt/C@NiCo (39.52 mV dec^{-1}), indicating the excellent HER reaction kinetics of Ir-nc@m-NiCo. Electrochemical impedance spectroscopy (EIS) was performed to assess the HER kinetics of Ir-nc@m-NiCo further. The Nyquist plots of Ir-nc@m-NiCo show a much lower charge-transfer impedance as compared with Ir-nc@Co and Ir-nc@Ni (Fig. S5†), supporting the fast electron transfer ability of Ir-nc@m-NiCo. The potential at 10 mA cm^{-2} and the corresponding Tafel slope of Ir-nc@m-NiCo are appreciably superior to those of previously reported precious metal catalysts and other non-precious HER electrocatalysts in 1.0 M KOH (Fig. 4d and Table S1†). The systematic investigations of the HER activity of Ir-nc@m-NiCo, Ir-nc@Co, and Ir-nc@Ni, together with material characterization by SEM, high-resolution TEM, XRD, and XPS, conclude that the Ir nanocluster coordinated with atomic Ni and Co contributes to providing the active sites in Ir-nc@m-NiCo.

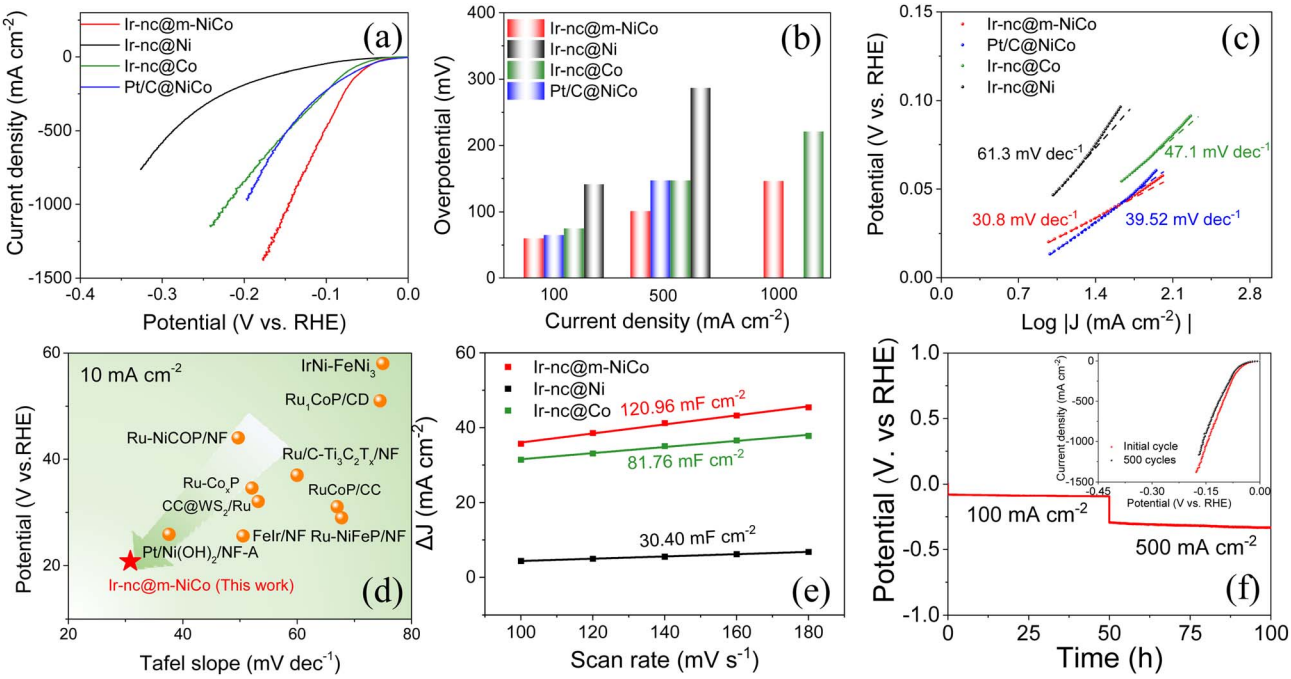

Fig. 4 (a) HER polarization curves of Ir-nc@m-NiCo, Ir-nc@Co, Ir-nc@Ni, and Pt/C@NiCo. (b) Comparison of overpotential (η) to drive a current density of 100, 500, and 1000 mA cm^{-2} between Ir-nc@m-NiCo, Ir-nc@Co, Ir-nc@Ni, and Pt/C@NiCo. (c) The corresponding Tafel plots for Ir-nc@m-NiCo, Ir nc@Co, Ir nc@Ni and Pt/C@NiCo. (d) Comparison of overpotential (@ 10 mA cm^{-2}) and Tafel slope for various state-of-the-art HER catalysts in alkaline medium. (e) ECSAs of Ir-nc@m-NiCo. (f) Chronopotentiometry curve with Ir-nc@m-NiCo as the electrode at 100 and 500 cm^{-2} without *iR* compensation. Inset shows the polarization curves of Ir-nc@m-NiCo before and after 500 cycles with *iR* compensation.

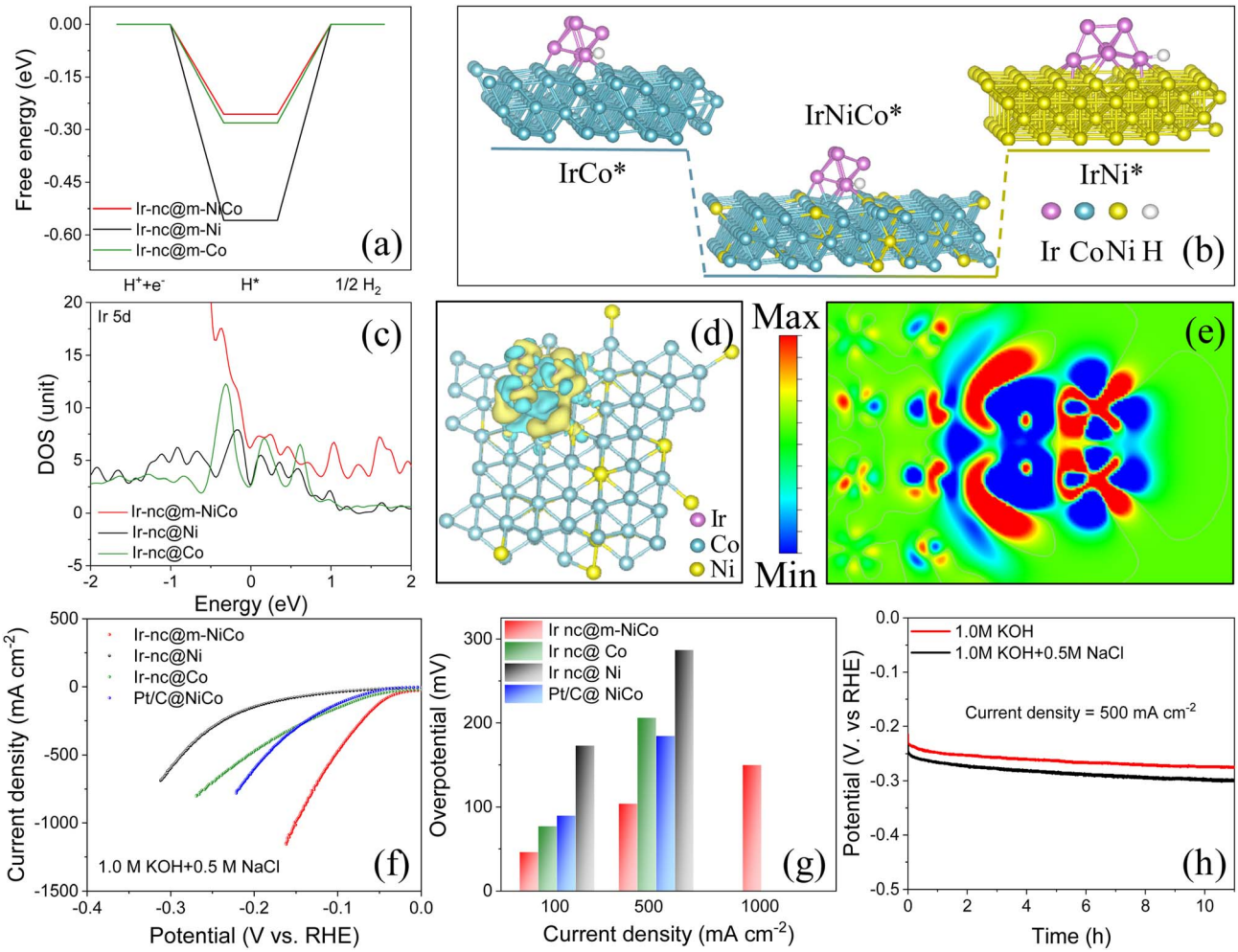

Fig. 5 (a) Calculated free-energy change and (b) hydrogen adsorption energies for Ir-nc@m-NiCo. (c) Calculated density of states graphs of Ir 5d for Ir-nc@m-NiCo, Ir-nc@Co, and Ir-nc@Ni. (d) Charge density of Ir-nc@m-NiCo. Yellow represents the electron accumulation area and blue represents the electron dissipation area. (e) Electron localization function (ELF) of Ir-nc@m-NiCo. (f) HER polarization curves of Ir-nc@m-NiCo, Ir nc@Co, Ir nc@Ni, and Pt/C@NiCo in alkaline saline electrolytes. (g) Comparison of overpotential (η) to drive a current density of 100, 500, and 1000 mA cm^{-2} between Ir-nc@m-NiCo, Ir nc@Co, Ir nc@Ni and Pt/C@NiCo in alkaline saline electrolytes. (h) Long-term stability test at 500 mA cm^{-2} on the Ir-nc@m-NiCo electrode in alkaline saline solutions.

To identify the effect of Ir nanocluster coordinated on macropores NiCo on the outstanding HER performance, we measured the electrochemical double-layer capacitance (C_{dl}) to evaluate the electrochemical surface area (ECSA) of Ir-nc@m-NiCo. As shown in Fig. 4e and S6,† Ir-nc@m-NiCo shows a higher C_{dl} of 120.96 mF cm^{-2}, compared with Ir-nc@Co (81.76 mF cm^{-2}) and Ir-nc@Ni (30.40 mF cm^{-2}), illustrating that Ir-nc@m-NiCo possesses an extraordinary activity with a larger ECSA and more accessible active sites attributed to the macroporous structure. For the clarification of the inherent HER activity of Ir-nc@m-NiCo, the ECSA normalized polarization curve was explored, and it was found that the intrinsic activity of Ir-nc@m-NiCo was still much higher than that of Ir-nc@Co and Ir-nc@Co (Fig. S7†). As shown in Fig. S8† for the multi-step chronopotentiometry curve of Ir-nc@m-NiCo (without *iR* compensation), the starting current density is 200 mA cm^{-2} at −0.14 V for a test period of 100 s per stage, up to 1000 mA cm^{-2}. The voltage at each stage almost remains unchanged, suggesting the outstanding mass transport properties and mechanical toughness of Ir-nc@m-NiCo. As durability is another adequate standard to assess the electrocatalytic ability of Ir-nc@m-NiCo, continuous electrochemical cycling tests were performed for 500 cycles (inside Fig. 4f). The current loss in the LSV curve over 500 CV cycles is negligible, suggesting the excellent durability of Ir-nc@m-NiCo. Furthermore, Ir-nc@m-NiCo exhibits its long-term durability with a minor potential decrease during consecutive current output at 100 and 500 mA cm^{-2} over 100 h under alkaline conditions (Fig. 4f).[28–37] Subsequently, the content of the noble-metal element (Ir) in the electrolyte was investigated. Through the ICP-MS test results, we found that the content of Ir in the electrolyte is extremely low, below the detection limit. The results further confirm the outstanding stability of this as-prepared catalyst. Moreover, the XRD peaks of Ir-nc@m-NiCo largely remain the same as before the stability test and, thus, the results reveal its high durability (Fig. S9†). The higher stability of Ir clusters on the NiCo support

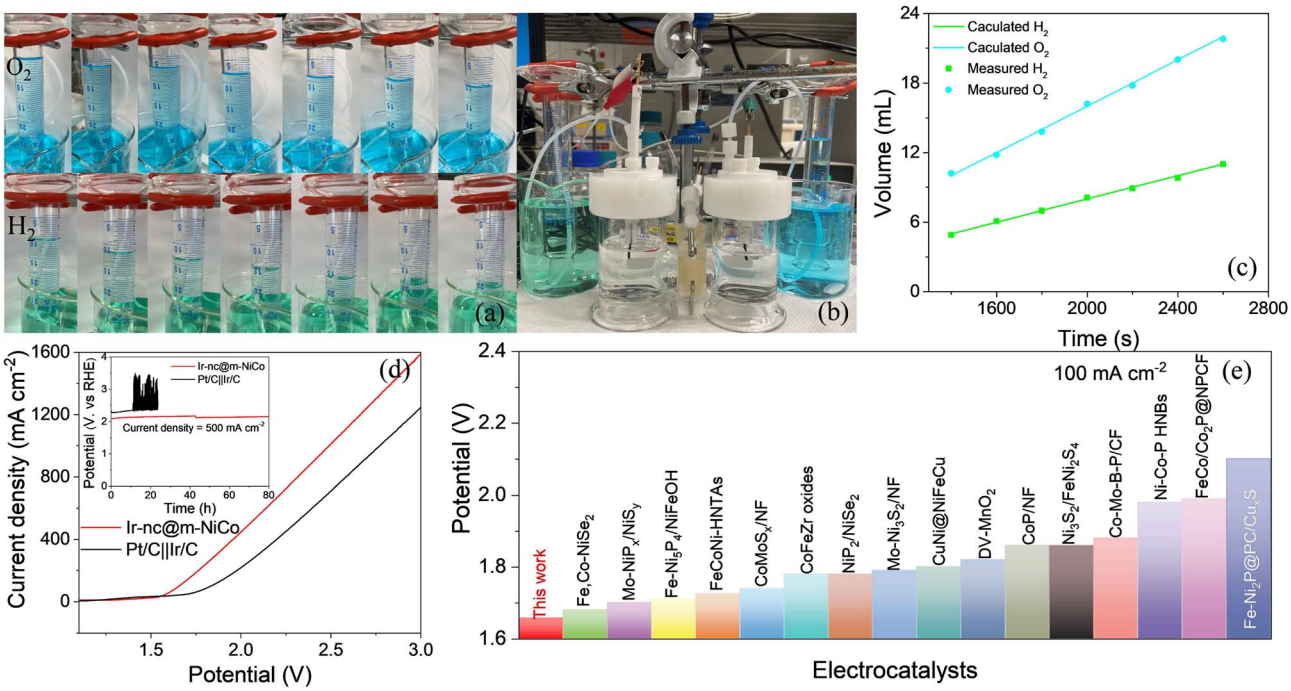

Fig. 6 (a) H_2 and O_2 collected and (b) gas measuring device. (c) The volume of gas at the beginning and 1200, 1600, 2000, 2400, and 2800 seconds of the water electrolysis process. (d) Polarization curves of bifunctional Ir-nc@m-NiCo and Pt/C//Ir/C for overall-water-splitting. Inset shows an 80 hour stability test at 500 mA cm^{-2}. (e) HER polarization curves of Ir-nc@m-NiCo in 1.0 M KOH and 0.5 M NaCl solution. (f) Comparison of the voltages required to achieve a current density of 100 mA cm^{-2} for overall water splitting between Ir-nc@m-NiCo and other self-supported bifunctional electrocatalysts.

can be ascribed to stronger interactions between Ir clusters and the NiCo support.

From the outstanding performance of the HER, it can be found that Ir-nc@m-NiCo can effectively boost HER activity, exceeding the effects of Ir-nc@Co and Ir-nc@Ni. All these results imply that Ir coordinated with Ni and Co could be the real active site in Ir-nc@m-NiCo. Therefore, we further aimed to identify the actual active sites at the atomic level for the HER on Ir-nc@m-NiCo. The Tafel slope of Ir-nc@m-NiCo is 30.8 mV dec^{-1} ($\approx$29 mV dec^{-1}), so the possible HER mechanism on the catalyst surface will be Volmer–Tafel.[38] The (111) plane is the most thermally stable and available in the experiment.[11] Thus, an Ir6 nanocluster with a thermally stable (111) plane is embedded in the NiCo structure as a simplified model, mainly coordinated with Co or Ni atoms (Fig. S10†). As shown in Fig. 5a and b, the Ir site coordinated with both Ni and Co (IrNiCo*) exhibits near-zero Gibbs free energy ΔG_{H^*} (−0.256 eV), slightly smaller than that of Ir sites coordinated with Co atoms (IrCo*) (−0.281 eV), and significantly lower than that of Ir sites coordinated with Ni atoms (IrNi*) (−0.559 eV), indicating its faster electron-transfer and thus a higher hydrogen release rate during the HER process. As shown in Fig. 5c, the partial density of states (PDOS) of Ir sites in Ir-nc@m-NiCo shows higher electronic states near the Fermi level (E_f), compared with the Ir sites in Ir-nc@Co and Ir-nc@Ni. Activating Ir sites can optimize the charge transfer and improve the HER catalytic activity. It is found that the d-band center (ε_d) of Ir in Ir-nc@m-NiCo shifts to lower energy compared with Ir-nc@Co and Ir-nc@Ni, indicating more electron transfer from Ni and Co to Ir. Furthermore, the accumulation of electrons on Ir facilitates the acceleration of the Heyrovsky step, resulting in the adjustment of the free energy of H* desorption towards the desired value. Consequently, this weakens the adsorption of H* (Fig. S11†).[7,39] The charge density difference of Ir-nc@m-NiCo was simulated to further reveal the excellent HER performance. As shown in Fig. 5d, e and S12,† a noticeable charge accumulated around Ir, while the charge around Co and Ni atoms is significantly reduced, implies electron transfer from Ni and Co to Ir in Ir-nc@m-NiCo, which is in good agreement with the results of XPS. This electron redistribution behavior can optimize the active H species adsorption energy, thus enhancing the catalytic activity. All these calculated results manifest that IrNiCo* can enhance the HER activity.[40]

Furthermore, we conducted HER experiments, including all of the prepared samples in alkaline saline electrolytes (1.0 M KOH + 0.5 M NaCl solutions). As shown in Fig. 5f, the Ir-nc@m-NiCo HER electrocatalyst in 1.0 M KOH seawater electrolyte can reach 500 and 1000 mA cm^{-2} with overpotentials of 104 and 150 mV, respectively. The overpotentials needed for Ir-nc@m-NiCo and other HER electrocatalysts to drive current densities of 100, 500, and 1000 mA cm^{-2} in 1.0 M KOH seawater electrolytes are presented in Fig. 5g. To verify the stability of this Ir-nc@m-NiCo electrocatalyst in seawater, we also conducted HER stability tests in the alkaline saline electrolytes. As shown in Fig. 5h, Ir-nc@m-NiCo could work continuously for over ten hours at a current density of 500 mA cm^{-2}.

Oxygen evolution reaction (OER) performance tests of different catalysts were conducted. Ir-nc@m-NiCo can reach 10 mA cm^{-2} at a potential of 1.42 V, with a Tafel slope of 68.29 mV dec^{-1} and a large C_{dl} of 201.28 mF cm^{-2} (Fig. S13–S17†), exhibiting extraordinary OER activity, even superior to that of commercial Ir/C@NiCo. Ir-nc@m-NiCo can work as a bifunctional catalyst for overall water splitting based on its outstanding HER and OER performance. We conducted an experiment to measure hydrogen and oxygen generated from the surface of Ir-nc@m-NiCo during the overall water-splitting process. The apparatus was set up with an H-type electrolytic cell using a Nafion membrane as a separator through the drainage method. As shown in Fig. 6a and b, hydrogen and oxygen are released from the device using 1.0 M KOH electrolyte and the H_2 and O_2 volumes are 24 and 12 mL, respectively (ratio = 2 : 1). The results prove that the Faraday efficiency of Ir-nc@m-NiCo driving the overall water splitting is almost 100%, indicating the extremely high selectivity of such a bifunctional catalyst for water electrolysis in alkaline media (Fig. 6c). In Fig. 6d, the bifunctional Ir-nc@m-NiCo electrocatalyst outperforms other electrocatalysts in overall water splitting with only 1.67, 2.05, and 2.48 V to reach high current densities of 100, 500, and 1000 mA cm^{-2} in 1.0 M KOH electrolyte, respectively. Meanwhile, these values surpass those of the precious metal catalysts of Ir/C//Pt/C (1.83, 2.30, and 2.77 V) and exceed those of other self-supported bifunctional electrocatalysts as shown in Fig. 6e.[40–55] The long-term stability of Ir-nc@m-NiCo in electrochemical water splitting is confirmed at a high current density of 500 mA cm^{-2} for >80 h with negligible degradation (Fig. 6d).

Conclusion

In summary, Ir nanoclusters coordinated with macroporous NiCo foam have been developed through a facile corrosion engineering method. Ir-nc@m-NiCo exhibits outstanding HER performance, which requires low voltages of 101 and 146 mV to reach high current densities of 500 and 1000 mA cm^{-2}, respectively. The performance is superior to that of the benchmark commercial Pt/C@NiCo. As a result, Ir-nc@m-NiCo functioning as both cathode and anode electrodes can drive 100 and 500 mA cm^{-2} current densities at ultralow cell voltages of only 1.67 and 2.05 V, respectively. DFT calculations reveal that the Ir site coordinated with Ni and Co changes the adsorption energy of hydrogen and optimizes ΔG_{H^*}. The effects are favorable to the HER process. Ir-nc@m-NiCo presented in this work provides a promising way to synthesize precious metal coordinated with transition metal catalysts towards practical applications for green hydrogen production, as well as the electrochemical O_2 reduction, CO_2 reduction, and N_2 reduction reactions.

Conflicts of interest

There are no conflicts to declare.

Acknowledgements

This work was supported by the Research Grants Council of the Hong Kong Special Administrative Region, China (Project no. CityU 11206520) and the National Natural Science Foundation of China (no. 22102015).

References

1 L. Wang, Y. Hao, L. Deng, F. Hu, S. Zhao, L. Li and S. Peng, *Nat. Commun.*, 2022, **13**, 5785.
2 J. Zhang, L. Zhang, J. Liu, C. Zhong, Y. Tu, P. Li, L. Du, S. Chen and Z. Cui, *Nat. Commun.*, 2022, **13**, 5497.
3 J. Liu, J. Zhou and M. K. H. Leung, *ACS Appl. Mater. Interfaces*, 2022, **14**, 4399–4408.
4 Y. Liu, J. Ding, F. Li, X. Su, Q. Zhang, G. Guan, F. Hu, J. Zhang, Q. Wang, Y. Jiang, B. Liu and H. B. Yang, *Adv. Mater.*, 2023, **35**, 2207114.
5 K. Chen, Y. Huan, W. Quan, L. Zhu, J. Fu, J. Hu, F. Cui, F. Zhou, X. Wang, M. Li and Y. Zhang, *ACS Energy Lett.*, 2022, **7**, 3675–3684.
6 C. Li and J.-B. Baek, *ACS Omega*, 2020, **5**, 31–40.
7 Y. Sun, Z. Xue, Q. Liu, Y. Jia, Y. Li, K. Liu, Y. Lin, M. Liu, G. Li and C.-Y. Su, *Nat. Commun.*, 2021, **12**, 1369.
8 J. Yuan, X. Cheng, H. Wang, C. Lei, S. Pardiwala, B. Yang, Z. Li, Q. Zhang, L. Lei, S. Wang and Y. Hou, *Nano-Micro Lett.*, 2020, **12**, 104.
9 X. Cheng, Y. Li, L. Zheng, Y. Yan, Y. Zhang, G. Chen, S. Sun and J. Zhang, *Energy Environ. Sci.*, 2017, **10**, 2450–2458.
10 U. Lačnjevac, R. Vasilić, A. Dobrota, S. Đurđić, O. Tomanec, R. Zbořil, S. Mohajernia, N. T. Nguyen, N. Skorodumova, D. Manojlović, N. Elezović, I. Pašti and P. Schmuki, *J. Mater. Chem. A*, 2020, **8**, 22773–22790.
11 M. Sheng, B. Jiang, B. Wu, F. Liao, X. Fan, H. Lin, Y. Li, Y. Lifshitz, S.-T. Lee and M. Shao, *ACS Nano*, 2019, **13**, 2786–2794.
12 F. Li, G.-F. Han, H.-J. Noh, J.-P. Jeon, I. Ahmad, S. Chen, C. Yang, Y. Bu, Z. Fu, Y. Lu and J.-B. Baek, *Nat. Commun.*, 2019, **10**, 4060.
13 L.-W. Chen, X. Guo, R.-Y. Shao, Q.-Q. Yan, L.-L. Zhang, Q.-X. Li and H. W. Liang, *Nano Energy*, 2021, **81**, 105636.
14 Q. Q. Chen, C. C. Hou, C.-J. Wang, X. Yang, R. Shi and Y. Chen, *Chem. Commun.*, 2018, **54**, 6400–6403.
15 W. Lin, Y. R. Lu, W. Peng, M. Luo, T.-S. Chan and Y. Tan, *J. Mater. Chem. A*, 2022, **10**, 9878–9885.
16 X. Guo, X. Wan, Q. Liu, Y. Li, W. Li and J. Shui, *eScience*, 2022, **2**, 304–310.
17 Q. Hu, K. Gao, X. Wang, H. Zheng, J. Cao, L. Mi, Q. Huo, H. Yang, J. Liu and C. He, *Nat. Commun.*, 2022, **13**, 3958.
18 J. Cai, R. Javed, D. Ye, H. Zhao and J. Zhang, *J. Mater. Chem. A*, 2020, **8**, 22467–22487.
19 W. Xie, T. Yu, Z. Ou, J. Zhang, R. Li, S. Song and Y. Wang, *ACS Sustain. Chem. Eng.*, 2020, **8**, 9070–9078.
20 Z. Liu, X. Yang, G. Hu and L. Feng, *ACS Sustain. Chem. Eng.*, 2020, **8**, 9136–9144.
21 Y. Pei, B. Rezaei, X. Zhang, Z. Li, H. Shen, M. Yang and J. Wang, *Mater. Chem. Front.*, 2020, **4**, 2665–2672.
22 T. Sun, J. Cao, J. Dong, H. Du, H. Zhang, J. Chen and L. Xu, *Int. J. Hydrogen Energy*, 2017, **42**, 6637–6645.
23 Q. Wang, C.-Q. Xu, W. Liu, S.-F. Hung, H. Bin Yang, J. Gao, W. Cai, H. M. Chen, J. Li and B. Liu, *Nat. Commun.*, 2020, **11**, 4246.

24 H. You, D. Wu, D. Si, M. Cao, F. Sun, H. Zhang, H. Wang, T.-F. Liu and R. Cao, *J. Am. Chem. Soc.*, 2022, **144**, 9254–9263.
25 C. Wang, P. Zhai, M. Xia, Y. Wu, B. Zhang, Z. Li, L. Ran, J. Gao, X. Zhang, Z. Fan, L. Sun and J. Hou, *Angew. Chem., Int. Ed.*, 2021, **60**, 27126–27134.
26 X. Zhao, Y. Chang, J. Ji, J. Jia and M. Jia, *RSC Adv.*, 2021, **11**, 33179–33185.
27 Q. Wang, X. Huang, Z. L. Zhao, M. Wang, B. Xiang, J. Li, Z. Feng, H. Xu and M. Gu, *J. Am. Chem. Soc.*, 2020, **142**, 7425–7433.
28 Y. Wang, G. Qian, Q. Xu, H. Zhang, F. Shen, L. Luo and S. Yin, *Appl. Catal., B*, 2021, **286**, 119881.
29 H. Song, M. Wu, Z. Tang, J. S. Tse, B. Yang and S. Lu, *Angew. Chem., Int. Ed.*, 2021, **60**, 7234–7244.
30 D. Chen, R. Lu, Z. Pu, J. Zhu, H.-W. Li, F. Liu, S. Hu, X. Luo, J. Wu, Y. Zhao and S. Mu, *Appl. Catal., B*, 2020, **279**, 119396.
31 A. Kong, M. Peng, H. Gu, S. Zhao, Y. Lv, M. Liu, Y. Sun, S. Dai, Y. Fu, J. Zhang and W. Li, *Chem. Eng. J.*, 2021, **426**, 131234.
32 Y. Chen, D. Wang, T. Meng, Z. Xing and X. Yang, *ACS Appl. Energy Mater.*, 2022, **5**, 697–704.
33 Y. Lin, M. Zhang, L. Zhao, L. Wang, D. Cao and Y. Gong, *Appl. Surf. Sci.*, 2021, **536**, 147952.
34 J. Li, Y. Li, J. Wang, C. Zhang, H. Ma, C. Zhu, D. Fan, Z. Guo, M. Xu, Y. Wang and H. Ma, *Adv. Funct. Mater.*, 2022, **32**, 2109439.
35 Y. Gu, Y. Wang, J. Shi, M. Yang, Y. Rui, W. An and Y. Men, *Int. J. Hydrogen Energy*, 2020, **45**, 27067–27077.
36 J. Chen, Y. Wang, G. Qian, T. Yu, Z. Wang, L. Luo, F. Shen and S. Yin, *Chem. Eng. J.*, 2021, **421**, 129892.
37 C. Wang and L. Qi, *ACS Mater. Lett.*, 2021, **3**, 1695–1701.
38 S. Sultan, J. N. Tiwari, A. N. Singh, S. Zhumagali, M. Ha, C. W. Myung, P. Thangavel and K. S. Kim, *Adv. Energy Mater.*, 2019, **9**, 1900624.
39 Y. Zheng, Y. Jiao, M. Jaroniec and S. Z. Qiao, *Angew Chem. Int. Ed. Engl.*, 2015, **54**, 52–65.
40 E. Hu, Y. Feng, J. Nai, D. Zhao, Y. Hu and X. W. Lou, *Energy Environ. Sci.*, 2018, **11**, 872–880.
41 D. Cao, H. Xu and D. Cheng, *Appl. Catal., B*, 2021, **298**, 120600.
42 L. Huang, D. Chen, G. Luo, Y.-R. Lu, C. Chen, Y. Zou, C.-L. Dong, Y. Li and S. Wang, *Adv. Mater.*, 2019, **31**, 1901439.
43 C. F. Li, J. W. Zhao, L. J. Xie, J. Q. Wu and G. R. Li, *Appl. Catal., B*, 2021, **291**, 119987.
44 H. Li, S. Chen, Y. Zhang, Q. Zhang, X. Jia, Q. Zhang, L. Gu, X. Sun, L. Song and X. Wang, *Nat. Commun.*, 2018, **9**, 2452.
45 J. Liu, Y. Gao, X. Tang, K. Zhan, B. Zhao, B. Y. Xia and Y. Yan, *J. Mater. Chem. A*, 2020, **8**, 19254–19261.
46 Y. Liu, H. T. D. Bui, A. R. Jadhav, T. Yang, S. Saqlain, Y. Luo, J. Yu, A. Kumar, H. Wang, L. Wang, V. Q. Bui, M. G. Kim, Y. D. Kim and H. Lee, *Adv. Funct. Mater.*, 2021, **31**, 2010718.
47 X. Luo, P. Ji, P. Wang, R. Cheng, D. Chen, C. Lin, J. Zhang, J. He, Z. Shi, N. Li, S. Xiao and S. Mu, *Adv. Energy Mater.*, 2020, **10**, 1903891.
48 X. Shan, J. Liu, H. Mu, Y. Xiao, B. Mei, W. Liu, G. Lin, Z. Jiang, L. Wen and L. Jiang, *Angew. Chem., Int. Ed.*, 2020, **59**, 1659–1665.
49 Q. Shi, Q. Liu, Y. Ma, Z. Fang, Z. Liang, G. Shao, B. Tang, W. Yang, L. Qin and X. Fang, *Adv. Energy Mater.*, 2020, **10**, 1903854.
50 Y. Sun, K. Xu, Z. Wei, H. Li, T. Zhang, X. Li, W. Cai, J. Ma, H. J. Fan and Y. Li, *Adv. Mater.*, 2018, **30**, 1802121.
51 D. T. Tran, H. T. Le, V. H. Hoa, N. H. Kim and J. H. Lee, *Nano Energy*, 2021, **84**, 105861.
52 J. Wang, M. Zhang, G. Yang, W. Song, W. Zhong, X. Wang, M. Wang, T. Sun and Y. Tang, *Adv. Funct. Mater.*, 2021, **31**, 2101532.
53 Y. Wei, P. Zou, Y. Yue, M. Wang, W. Fu, S. Si, L. Wei, X. Zhao, G. Hu and H. L. Xin, *ACS Appl. Mater. Interfaces*, 2021, **13**, 20024–20033.
54 Y. Wu, Y. Li, M. Yuan, H. Hao, X. San, Z. Lv, L. Xu and B. Wei, *Chem. Eng. J.*, 2022, **427**, 131944.
55 L. Yang, L. Huang, Y. Yao and L. Jiao, *Appl. Catal., B*, 2021, **282**, 119584.

